



Title	Plasmonic mesostructures with aligned hotspots on highly oriented mesoporous silica films
Author(s)	Murai, Shunsuke; Uno, Shiguma; Kamakura, Ryosuke; Ishii, Satoshi; Nagao, Tadaaki; Fujita, Koji; Tanaka, Katsuhisa
Citation	Optical Materials Express, 6(9), 2824-2833 https://doi.org/10.1364/OME.6.002824
Issue Date	2016-09-01
Doc URL	http://hdl.handle.net/2115/72125
Rights	©2016 Optical Society of America]. Users may use, reuse, and build upon the article, or use the article for text or data mining, so long as such uses are for non-commercial purposes and appropriate attribution is maintained. All other rights are reserved.
Type	article
File Information	ome6-9_2824-2833.pdf



[Instructions for use](#)

Plasmonic mesostructures with aligned hotspots on highly oriented mesoporous silica films

SHUNSUKE MURAI,^{1,2,*} SHIGUMA UNO,¹ RYOSUKE KAMAKURA,¹ SATOSHI ISHII,^{3,4} TADAAKI NAGAO,^{3,4} KOJI FUJITA,¹ AND KATSUHISA TANAKA¹

¹Department of Material Chemistry, Graduate School of Engineering, Kyoto University, Katsura, Nishikyo-ku, Kyoto, 615-8510, Japan

²PRESTO, Japan Science and Technology Agency (JST), Kawaguchi, Saitama 332-0012, Japan

³International Center for Materials Nanoarchitectonics (MANA), National Institute for Materials Science (NIMS), Tsukuba, Ibaraki 305-0044, Japan

⁴Core Research for Evolutional Science and Technology (CREST), Japan Science and Technology Agency (JST), Kawaguchi, Saitama, 332-0012 Japan

*murai@dipole7.kuic.kyoto-u.ac.jp

Abstract: Gold mesostructures are fabricated by oblique angle deposition on highly oriented mesoporous silica (MPS) thin films utilizing the periodic surface corrugation on the scale of 10 nm as a prepattern for controlled deposition. Scanning electron microscopy analysis clarified that the mesostructures comprised an array of interconnected gold nanorods oriented in plane to form meso gratings. We measured the surface enhanced Raman scattering (SERS) to demonstrate that the nanosized gaps between the rods act as hotspots. Although the sample was as thin as 8.0 nm, large SERS signals appeared because of the very narrow gaps (< 2 nm). The spatial mapping confirmed the uniform distribution of hotspots over the sample.

©2016 Optical Society of America

OCIS codes: (240.6680) Surface plasmons; (160.6060) Solgel; (310.1860) Deposition and fabrication; (240.6695) Surface-enhanced Raman scattering.

References and links

1. S. A. Maier, *Plasmonics: Fundamentals and Applications* (Springer, 2007).
2. J. A. Schuller, E. S. Barnard, W. Cai, Y. C. Jun, J. S. White, and M. L. Brongersma, "Plasmonics for extreme light concentration and manipulation," *Nat. Mater.* **9**(3), 193–204 (2010).
3. R. K. Chang and T. A. Furtak, eds., *Surface-enhanced Raman Scattering* (Plenum, 1982).
4. J. J. Lasema, ed., *Modern Techniques in Raman Spectroscopy* (John Wiley & Sons, 1996).
5. A. M. Michaels, M. Nirmal, and L. E. Brus, "Surface enhanced Raman spectroscopy of individual rhodamine 6G molecules on large Ag nanocrystals," *J. Am. Chem. Soc.* **121**(43), 9932–9939 (1999).
6. S. Nie and S. R. Emory, "Probing Single molecules and single nanoparticles by surface-enhanced Raman scattering," *Science* **275**(5303), 1102–1106 (1997).
7. M. Moskovits, "Surface-enhanced Raman spectroscopy: a brief retrospective," *J. Raman Spectrosc.* **36**(6-7), 485–496 (2005).
8. T. Okamoto, F. H'Dhili, and S. Kawata, "Towards plasmonic bandgap laser," *Appl. Phys. Lett.* **85**(18), 3968–3970 (2004).
9. S. Kühn, U. Håkanson, L. Rogobete, and V. Sandoghdar, "Enhancement of single-molecule fluorescence using a gold nanoparticle as an optical nanoantenna," *Phys. Rev. Lett.* **97**(1), 017402 (2006).
10. P. Anger, P. Bharadwaj, and L. Novotny, "Enhancement and quenching of single-molecule fluorescence," *Phys. Rev. Lett.* **96**(11), 113002 (2006).
11. S. Kim, J. Jin, Y. J. Kim, I. Y. Park, Y. Kim, and S. W. Kim, "High-harmonic generation by resonant plasmon field enhancement," *Nature* **453**(7196), 757–760 (2008).
12. C. Leordean, B. Marta, A. M. Gabudean, M. Focsan, I. Botiz, and S. Astilean, "Fabrication of highly active and cost effective SERS plasmonic substrates by electrophoretic deposition of gold nanoparticles on a DVD template," *Appl. Surf. Sci.* **349**, 190–195 (2015).
13. X. Y. Zhang, A. Hu, T. Zhang, W. Lei, X. J. Xue, Y. Zhou, and W. W. Duley, "Self-assembly of large-scale and ultrathin silver nanoplate films with tunable plasmon resonance properties," *ACS Nano* **5**(11), 9082–9092 (2011).
14. K. Okamoto, B. Lin, K. Imazu, A. Yoshida, K. Toma, M. Toma, and K. Tamada, "Tuning colors of silver nanoparticle sheets by multilayered crystalline structures on metal substrates," *Plasmonics* **8**(2), 581–590 (2013).
15. L. Malassis, P. Massé, M. Tréguer-Delapierre, S. Mornet, P. Weisbecker, V. Kravets, A. Grigorenko, and P. Barois, "Bottom-up fabrication and optical characterization of dense films of meta-atoms made of core-shell plasmonic nanoparticles," *Langmuir* **29**(5), 1551–1561 (2013).
16. M. Suzuki and Y. Taga, "Numerical study of the effective surface area of obliquely deposited thin films," *J. Appl. Phys.* **90**(11), 5599–5605 (2001).

17. M. Suzuki, T. Ito, and Y. Taga, "Photocatalysis of sculptured thin films of TiO₂," *Appl. Phys. Lett.* **78**(25), 3968–3970 (2001).
18. J. Parra-Barranco, F. J. García-García, V. Rico, A. Borrás, C. López-Santos, F. Frutos, A. Barranco, and A. R. González-Elipe, "Anisotropic in-plane conductivity and dichroic gold plasmon resonance in plasma-assisted ITO thin films e-beam-evaporated at oblique angles," *ACS Appl. Mater. Interfaces* **7**(20), 10993–11001 (2015).
19. L. Gonzalez-García, J. Parra-Barranco, J. Ramón Sanchez-Valencia, J. Ferrer, A. Mari-Cruz Garcia-Gutierrez, "Barranco, and A. R. Gonzalez-Elipe, "Tuning dichroic plasmon resonance modes of gold nanoparticles in optical thin films," *Adv. Funct. Mater.* **23**(13), 1655–1663 (2013).
20. J. R. Sanchez-Valencia, J. Toudert, A. Borrás, A. Barranco, R. Lahoz, G. F. de la Fuente, F. Frutos, and A. R. Gonzalez-Elipe, "Selective dichroic patterning by nanosecond laser treatment of Ag nanostructures," *Adv. Mater.* **23**(7), 848–853 (2011).
21. J. C. Hulthen and P. Van Duyn, "Nanosphere lithography: A materials general fabrication process for periodic particle array surfaces," *J. Vac. Sci. Technol.* **A 13**(3), 1553–1558 (1995).
22. H. Im, K. C. Bantz, S. H. Lee, T. W. Johnson, C. L. Haynes, and S. H. Oh, "Self-assembled plasmonic nanoring cavity arrays for SERS and LSPR biosensing," *Adv. Mater.* **25**(19), 2678–2685 (2013).
23. T. Kondo, H. Masuda, and K. Nishio, "SERS in ordered array of geometrically controlled nanodots obtained using anodic porous alumina," *J. Phys. Chem. C* **117**(6), 2531–2534 (2013).
24. H. H. Wang, C. Y. Liu, S. B. Wu, N. W. Liu, C. Y. Peng, T. H. Chan, C. F. Hsu, J. K. Wang, and Y. L. Wang, "Highly Raman-enhancing substrates based on silver nanoparticle arrays with tunable Sub-10 nm gaps," *Adv. Mater.* **18**(4), 491–495 (2006).
25. S. Biring, H. H. Wang, J. K. Wang, and Y. L. Wang, "Light scattering from 2D arrays of monodispersed Ag-nanoparticles separated by tunable nano-gaps: spectral evolution and analytical analysis of plasmonic coupling," *Opt. Express* **16**(20), 15312–15324 (2008).
26. J. Gu, W. Zhang, H. Su, T. Fan, S. Zhu, Q. Liu, and D. Zhang, "Morphology genetic materials templated from natural species," *Adv. Mater.* **27**(3), 464–478 (2015).
27. S. G. Park, C. Mun, M. Lee, T. Y. Jeon, H. S. Shim, Y. J. Lee, J. D. Kwon, C. S. Kim, and D. H. Kim, "3D Hybrid plasmonic nanomaterials for highly efficient optical absorbers and sensors," *Adv. Mater.* **27**(29), 4290–4295 (2015).
28. W. Zhu, M. G. Banaee, D. Wang, Y. Chu, and K. B. Crozier, "Lithographically fabricated optical antennas with gaps well below 10 nm," *Small* **7**(13), 1761–1766 (2011).
29. T. Yanagisawa, T. Shimizu, K. Kuroda, and C. Kato, "The Preparation of alkyltriethylammonium-kaneinite complexes and their conversion to microporous materials," *Bull. Chem. Soc. Jpn.* **63**(4), 988–992 (1990).
30. C. T. Kresge, M. E. Leonowicz, W. J. Roth, J. C. Vartuli, and J. S. Beck, "Ordered Mesoporous Molecular Sieves Synthesized by a Liquid-crystal template," *Nature* **359**(6397), 710–712 (1992).
31. H. Miyata and K. Kuroda, "Formation of a continuous mesoporous silica film with fully aligned mesochannels on a glass substrate," *Chem. Mater.* **12**(1), 49–54 (2000).
32. S. Hayase, Y. Kanno, M. Watanabe, M. Takahashi, K. Kuroda, and H. Miyata, "Heteroepitaxial formation of aligned mesostructured silica films with large structural periodicities from mixed surfactant systems," *Langmuir* **29**(23), 7096–7101 (2013).
33. M. Kitahara and K. Kuroda, "Preparation of highly controlled nanostructured Au within mesopores using reductive deposition in non-polar environments," *RSC Advances* **4**(52), 27201–27206 (2014).
34. G. Kawamura, I. Hayashi, H. Muto, and A. Matsuda, "Anisotropically assembled gold nanoparticles prepared using unidirectionally aligned mesochannels of silica film," *Scr. Mater.* **66**(7), 479–482 (2012).
35. C. Li, Ö. Dag, T. D. Dao, T. Nagao, Y. Sakamoto, T. Kimura, O. Terasaki, and Y. Yamauchi, "Electrochemical synthesis of mesoporous gold films toward mesospace-stimulated optical properties," *Nat. Commun.* **6**, 6608 (2015).
36. S. Vignolini, N. A. Yufa, P. S. Cunha, S. Guldin, I. Rushkin, M. Stefik, K. Hur, U. Wiesner, J. J. Baumberg, and U. Steiner, "A 3D optical metamaterial made by self-assembly," *Adv. Mater.* **24**(10), OP23–OP27 (2012).
37. S. Murai, S. Uno, R. Kamakura, K. Fujita, and K. Tanaka, "Plasmonic mesostructures prepared by oriented mesoporous materials as a template," *ECS Trans.* **69**(2), 117–121 (2015).
38. M. Kobayashi, Y. Kanno, and K. Kuroda, "Replication of ordered mesostructure on the surface of 2D hexagonal mesoporous silica film as exemplified by the formation of striped Cu nanopatterns," *Chem. Lett.* **43**(6), 846–848 (2014).
39. J. A. Thornton, "The microstructure of sputter deposited coatings," *J. Vac. Sci. Technol. A* **4**(6), 3059–3065 (1986).
40. S. Mahajan, R. M. Cole, J. D. Speed, S. H. Pelfrey, A. E. Russell, P. N. Bartlett, S. M. Barnett, and J. J. Baumberg, "Understanding the surface-enhanced Raman spectroscopy background," *J. Phys. Chem. C* **114**(16), 7242–7250 (2010).
41. S. K. Miller, A. Baiker, M. Meier, and A. Wokaun, "Surface-enhanced Raman scattering and the preparation of copper substrates for catalytic studies," *J. Chem. Soc., Faraday Trans. I* **80**(5), 1305–1312 (1984).

1. Introduction

Metallic nanostructures can interact strongly with light at the nanoscale through the collective oscillation of free electrons coupled to light waves, i.e., surface plasmon polariton (SPP) [1,2]. While dielectric-based photonic systems such as waveguides and photonic crystals can confine light in a volume comparable to the wavelength, SPPs can be confined to a volume

smaller than the diffraction limit. Nanosized spaces where light energy accumulates, such as sharp apexes of a single nanoparticle and gaps between two nanoparticles, are called hotspots. Hotspots are utilized to modulate and enhance optical processes to cause surface enhanced Raman scattering (SERS) [3–7], fluorescence enhancement [8–10], and high-harmonic generation [11], to name a few examples.

There have been a number of studies on the fabrication of structures to maximize the number density of hotspots by using either top-down or bottom-up approaches [7–28]. Here we focus on nanosized gaps between particles as hotspots since they act more efficiently than isolated nanoparticles. The simplest bottom-up approach to making such structures is to disperse and deposit metallic nanoparticles on substrates randomly to form aggregates and use the naturally formed gaps as hotspots [7,12,13]. This method works well to some extent; however, the spatial distribution of the gaps is random and uncontrollable. Alternatively, the Langmuir-Blodgett method provides a sophisticated way to prepare layers of nanoparticles with a designed gap size [14,15]. In most cases, the gaps are occupied by the surfactant that defines the gap size and suppresses aggregation. Thus, the gaps are unavailable for other molecules for further applications. The physical deposition method is advantageous for open gaps that are free from surfactants. Anisotropic deposition onto flat and/or prepatterned substrates is an established way of fabricating metallic micro- and nanostructures [16–20]. The fabrication process for nanogaps via physical deposition of metals through a close-packed monolayer of nanoparticles as a mask is referred to as nanosphere lithography (NSL) [21,22]. An anodic alumina membrane [23] also works well as a mask to define the gap structure. Certain techniques allow the fabrication of metallic structures with a characteristic size below 100 nm [24,25]. Even natural species have been found to offer useful templates [26]. However, even with bottom-up techniques, the fabrication of metallic structures with a characteristic gap size below 5 nm has not been conventionally achieved on a large scale.

Mesoporous silica (MPS) is a group of porous materials typically prepared by the sol-gel method. In general, three-dimensional structures are first constructed by self-assembled micelles of surfactants, which are then fixed by solidification of a silicon source via polycondensation [29,30]. Extraction of the surfactant leaves pores with a size defined by the micelle size, which is typically less than 10 nm. Thin films of MPS can be easily obtained by dip coating or spin coating. In particular, a pretreated substrate enables the preparation of highly oriented thin films with a honeycomb array of cylindrical pores aligned parallel to the surface [31,32]. Modification of the pores with metals via the chemical or electrochemical route has been attempted for MPS and other porous materials prepared by self-assembly [33–36]. Kawamura *et al.* infiltrated oriented mesopores with metals and examined the polarization-sensitive optical response [34]. Li *et al.* prepared mesoporous gold (Au) to demonstrate its SERS activity [35]. However, none of the previous studies used mesoporous materials as scaffolds for physical deposition to prepare mesostructures with designed open gaps.

In the present study, we used an MPS thin film as a prepatterned substrate to fabricate metallic mesostructures with the high density of gaps uniformly distributed over the sample. Our strategy is simple: oblique angle deposition of Au on the MPS thin film by utilizing an oriented surface corrugation as a prepattern [37]. A one-dimensional surface corrugation with a period of 10 nm allows fabrication of a grating-like array of Au nanorods with a thickness less than 10 nm, a unit length less than 100 nm, and a gap size less than 2 nm. The periodicity and the gap width can be controlled by the deposition angle. The Au mesostructure possesses in-plane anisotropy that can resolve the polarization of incoming light; optical transmission shows the excitation of localized SPPs for p-polarized light with the electric field oscillating across the gap, while no SPPs are excited for s-polarized light. Comparison with the simulation shows that the optical response can be understood by a model composed of discrete nanorods aligned in-plane, where the gaps between the nanorods act as hotspots. As a demonstration, SERS measurements have been taken to show the intense Raman signal only for p-polarized light. By using the flat Au film as a reference, the enhancement factor is estimated to be 10^9 .

2. Experimental

2.1 Preparation of mesoporous silica thin films

First, Brij56 (1.737 g) and Pluronic123 (P123, 2.523 g) were dissolved in 2-propanol (61.0 ml). Then, 0.1 mol/l hydrochloric acid (1.92 ml), water (2.4 ml), and tetraethoxysilane (TEOS, 10.7 ml) were added sequentially. The mixture was stirred for 2 h and used as a precursor solution. Separately, a silica glass substrate coated with a rubbing-treated poly(hexamethylenepyrromellitimide) film was prepared. The substrate was dip-coated with the precursor solution. The thin film was dried at room temperature and then heated in air at 400 °C for 2 h. The typical thickness of the MPS thin films was ca. 500 nm. The surface silica layer of the MPS thin film was etched away to expose the periodic structures of the oriented mesocylinders [38].

2.2 Preparation of the Au mesostructure by oblique angle deposition

Deposition of Au on the MPS thin films was performed with an electron-beam deposition apparatus equipped with a sample holder designed for oblique angle deposition. The MPS thin film on the substrate was placed on a stainless steel holder, which was cooled by circulating liquid (a mixture of water and ethylene glycol) at -9.5 °C, and the chamber was evacuated to less than 1×10^{-4} Pa. The distance between the holder and the source was 40 cm to ensure the unidirectional flux of species impinging onto the substrate. Prior to the deposition of Au, a thin layer (0.3 nm) of chromium (Cr) was deposited as an adhesive layer. The deposition angle, α , which was defined as the angle between the substrate normal and the incident direction of the deposition flux, was varied between 0 and 80°. The thickness and deposition rate were monitored using a quartz crystal monitor, which was placed normal to the direction of deposition flux. The surface morphology of the films was examined by scanning electron microscopy (SEM, SU8000, Hitachi).

2.3 Optical characterization and Raman scattering measurement

The zeroth-order optical transmission of the sample was measured by using a collimated beam from a halogen lamp with a beam diameter of ca. 0.5 mm as a light source. The sample was mounted on a computer-controlled rotation stage. The incident angle of the collimated beam was varied in the plane perpendicular to the long axis of the mesocylinders. The absolute zeroth-order transmittance was obtained by normalizing the transmission of the incident light through the sample to that through the silica glass substrate.

The SERS properties were examined using a custom-made confocal Raman microscope (WITec Alpha 300S) combined with a monochromator (Action SP2300, Princeton Instruments) and a CCD camera (Andor iDus DU-401A BR-DD-352). The samples were dipped in an ethanol solution of Nile blue A (5×10^{-3} – 5×10^{-12} mol/l) and dried prior to the measurements. Ethanol has good wettability with the sample surface (Au) and leaves a homogenous layer of the analyte when it evaporates, thus allowing for the comparison study. In the typical SERS measurement, a diode laser (WITec) operating at 785 nm (0.9 mW) was focused on the sample using a 100 × objective (0.9 NA-Olympus), and the signals were collected with a collection time of 0.2 s and integrated over 10 times. This condition was optimized for high-resolution spatial mapping. The spatial resolution of the SERS scanning was estimated to be 1 μm (64×64 pixels over a 20×20 μm scanning area).

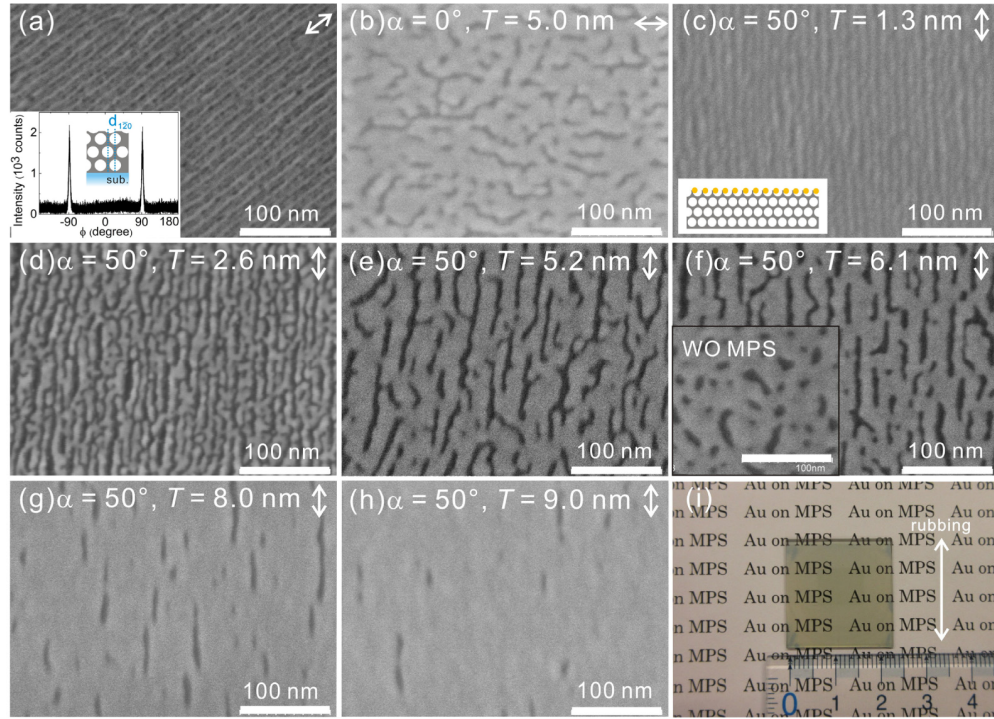


Fig. 1. SEM top-view images of the highly oriented MPS thin film (a), and Au mesostructures prepared on MPS by depositing Au at $\alpha = 0^\circ$ and estimated thickness $T = 5.0$ nm (b), and those at $\alpha = 50^\circ$ and $T = 1.3$ (c), 2.6 (d) 5.2 (e), 6.1 (f), 8.0 (g), and 9.0 nm (h). The inset in (a) shows in-plane X-ray ϕ scan monitoring of the peak from the $1\bar{2}0$ planes of the MPS thin film, that in (c) is the sketch of the cross section of the Au mesostructure, and that in (f) is the Au mesostructure prepared on the flat glass substrate by depositing Au at $\alpha = 50^\circ$ and $T = 6.1$ nm. The arrows in (a)–(h) indicate the direction of the long axis of the mesopores. (i) Optical image of the sample on MPS. The arrow indicates the direction of the rubbing treatment.

3. Results and discussion

3.1 Mesoscale structures of Au on MPS

Figure 1(a) is a top-view SEM image of the MPS thin film before the oblique angle deposition. Mesocylinders are macroscopically aligned parallel to the substrate surface due to the rubbing treatment [31]. The global alignment was also confirmed by in-plane X-ray diffraction; the ϕ scan monitoring ($1\bar{2}0$) planes, the plane normal to the surface (see the inset), showed peaks at $\phi = \pm 90^\circ$. The appearance of two peaks separated by 180° means that the mesochannels are aligned in-plane. The period of the structure is around 10 nm as examined from the SEM image. This indicates that the height of the surface corrugation is less than 10 nm. Figure 1(b) is the Au structure deposited on MPS at a deposition angle $\alpha = 0^\circ$ for an estimated thickness of $T = 5.0$ nm. The Au thickness was estimated from the relation $T = T_0 \times \cos\alpha$, where T_0 is the thickness obtained from the monitor equipped with the chamber. Brighter and continuous domains, which correspond to Au, extend over the surface corrugations of MPS, indicating that the surface corrugations of MPS are not high enough to prevent the diffusion of Au adatoms. Figures 1(c)–1(h) compare the morphology of Au deposited on MPS at a deposition angle $\alpha = 50^\circ$ and different T values. When $T = 1.3$ and 2.6 nm, (Figs. 1(c) and 1(d)) rod-like islands are observed, elongated along the underlying mesocylinders. When T is increased to 5.2 and 6.1 nm (Figs. 1(e) and 1(f)), the rods widen such that neighboring rods begin to connect to each other. Further increase in T causes dense interconnection of the rods to form a continuous surface with oriented nanocracks (Figs. 1(g)

and 1(h)). The nanocracks are fully covered by Au with further increase in T to 15.0 nm. The effect of the underlying MPS substrate is clear in comparison with the mesostructure of the Au films deposited directly on a flat silica substrate (inset in Fig. 1(f)), where the isotropic structure of Au with random pits is observed. The typical size of the samples is $2\text{ cm} \times 2\text{ cm}$ (see Fig. 1(i)), and the mesostructures are homogeneous over a single sample. We examined the local mesostructures at different spots on the sample surface by SEM to confirm no spot-to-spot variations in the mesostructure.

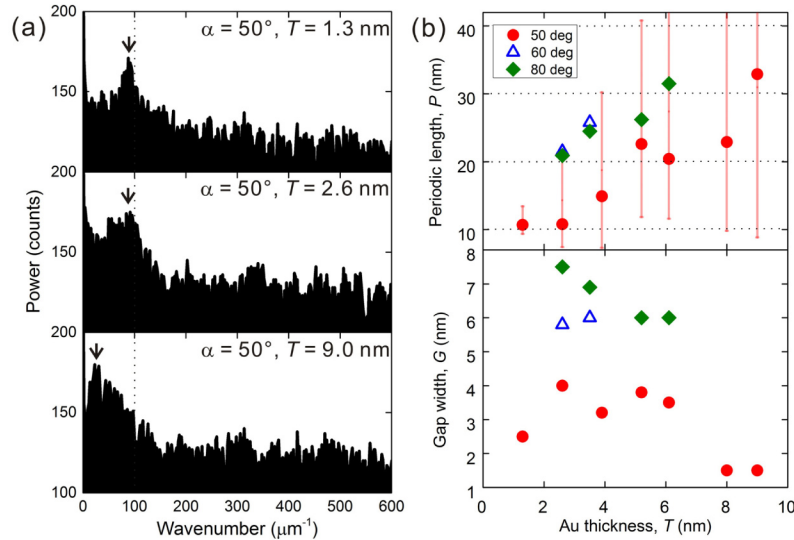


Fig. 2. (a) Power spectra obtained by two-dimensional Fourier transform of the SEM images of the samples deposited at $\alpha = 50^\circ$ and $T = 1.3$ (top), 2.6 (middle), and 9.0 nm (bottom), collected along the line perpendicular to the grating. The arrows indicate the peaks corresponding to the periodic length (P), and the vertical dotted line denotes $P = 10$ nm, the periodicity of the MPS. (b) Relation between the Au thickness T , and P (top panel) and the gap width, G (bottom panel). The circles, the triangles and the squares represent the data for the samples deposited at $\alpha = 50, 60$, and 80° , respectively. The vertical red lines denote the variation in P estimated for the samples with $\alpha = 50^\circ$ from the width of the peak in (a).

In Fig. 2, we extracted the structural parameters of the samples from the SEM images. First, the periodic length (P) was evaluated from the Fourier transform of the SEM image. Figure 2(a) shows typical Fourier power spectra. The peaks indicated by arrows are frequency-dependent components that reflect the P values of the structure. With the increase in T , the peak shifts to the lower wavenumber side, and becomes wider. This means that P becomes larger and more varied. Separately, we examined the gap ratio, defined as the ratio of the area occupied by the gap to the entire surface area, from the binarized SEM images. Finally, the gap width (G) was derived from the relation $G = P \times (\text{gap ratio})$, by assuming that the sample was a periodic array of nanorods, under which the gap ratio corresponds to G/P . Figure 2(b) shows P (top panel) and G (bottom) as a function of the Au thickness, T . Let us examine the variation in P for the samples with $\alpha = 50^\circ$. When the Au film is thin ($T \sim 1$ nm), P is around 10 nm, i.e., the pitch of the MPS substrate. With an increase in T , P deviates from that of the substrate and begins to increase. The red bars in Fig. 2(b) show the variations in P estimated from the widths of the peaks in the Fourier power spectra. The lower limit of P is fixed around 10 nm, while the upper limit increases far beyond 10 nm, as observed from the SEM images in Fig. 1. The increase in T also leads to a decrease in G .

According to the structure zone model (SZM) [39], the effect of diffusion can be classified in terms of the homologous temperature, T_h , which is defined as the ratio of the surface temperature during the deposition T_{sub} to the melting point of the deposited material T_{mp} , i.e., $T_h = T_{\text{sub}}/T_{\text{mp}}$. In the present case, where $T_h = 0.2$, the growth mechanism falls into

zone 1, in which surface diffusion is limited and the adatom shadowing effect controls the morphology. At the early stage of the deposition where the Au film is thin, the SZM holds, and the growth of narrow Au rods is observed on the edge of the surface corrugation of the substrate (see Fig. 1(c)). With increasing thickness, however, the diffusion of adatoms begins to dominate, leading to the increase in P and the decrease in G . In the present study, even in zone 1, the adatom diffusion on the surface defines the morphology on the order of 10 nm, which is one order smaller than typical structures prepared by oblique angle deposition.

Comparison between the samples with identical T shows that both P and G tend to be larger for larger α . This is related to the deposition rate. The flux of the depositing species per unit area varies with $\cos\alpha$, so that the deposition rate decreases with increasing α . For example, the deposition rate at $\alpha = 80^\circ$ is 3.7 times slower than that at $\alpha = 50^\circ$. When the deposition rate is slow, the Au atoms have sufficient time to diffuse on the surface, resulting in a coarsened structure with a larger P and consequently a larger G .

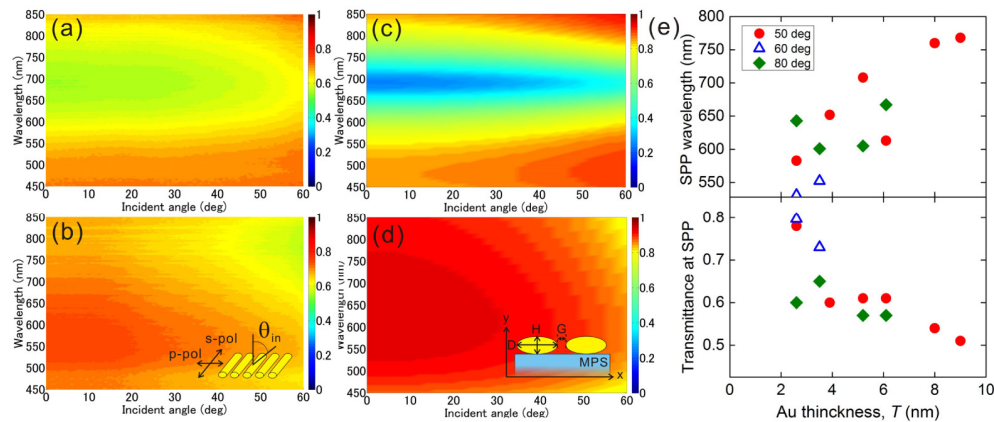


Fig. 3. Transmission spectra as a function of angle of incidence for the sample deposited at $\alpha = 50^\circ$ with $T = 5.2$ nm for (a) p- and (b) s-polarized light. The inset in (b) is the sketch of the experimental geometry. Simulated transmission spectra for (c) p- and (d) s-polarized light. The model is a two-dimensional periodic array of Au nanorods with diameter (D) = 24 nm, height (H) = 3.5 nm and gap width (G) of 4 nm, deposited on the 500 nm thick MPS substrate with an effective refractive index of 1.11. The inset in (d) shows the schematic illustration of the model with the coordinate x and y axes. (e) Relation between T , and the wavelength of SPP (top panel) and the optical transmission at the wavelength of SPP (bottom panel), for p-polarized light.

3.2 Optical transmission

Figure 3 summarizes the optical transmission results. For p-polarized light with the electric field of the incident light oscillating across the rods, a broad dip appears around a wavelength of $\lambda = 700$ nm, which is ascribed to the excitation of localized SPPs (Fig. 3(a)). In contrast, no apparent dip is observed for s-polarized light (Fig. 3(b)). The polarization dependence of the optical transmission was simulated by using the finite-element method (COMSOL Multiphysics). The two-dimensional model structure consists of Au nanorods with an ellipsoidal cross section (diameter $D = 24$ nm, height $H = 3.5$ nm) and a gap width $G = 4$ nm (see the inset in Fig. 3(d)). The nanorods are on a flat substrate with a refractive index of 1.11, which is the effective refractive index weighed by the volume fractions of silica and air. A periodic boundary condition was applied in the lateral direction, and a perfectly matched layer was set at the bottom of the model to eliminate the reflection from the boundary. A plane wave was incident from the top, and the transmitted light was monitored to calculate the optical transmission. The results show a dip only for p-polarized light, as shown in Figs. 3(c) and 3(d), which satisfactorily agrees with the experimental results. The simulation results indicate that the periodic nanorod array model explains the macroscopic optical response, although the prepared structure is not a perfect grating as in the model.

Figure 3(e) plots the SPP response for p-polarized light as a function of the Au thickness, T . With an increase in T , the resonant wavelength of the SPP is red-shifted because of the increase in the diameter of the rods (upper panel). The dip in transmittance grows deeper at the same time (bottom), because the excitation of SPPs becomes stronger with the increase in the amount of Au.

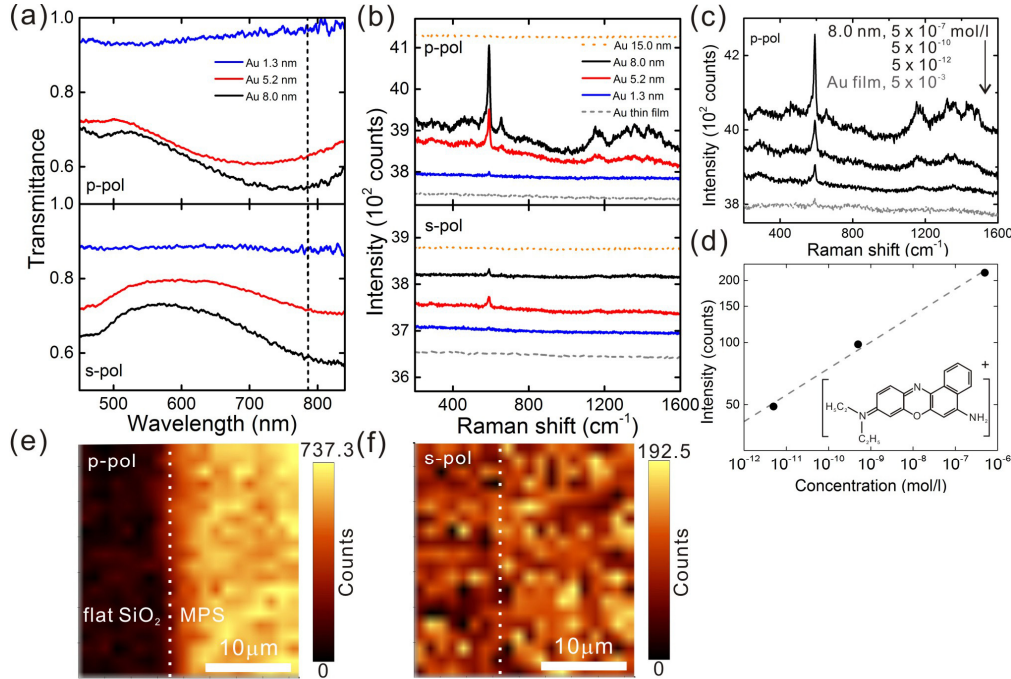


Fig. 4. (a) Transmission spectra at normal incidence for p- (top panel) and s- (bottom) polarized light. The samples were deposited at $\alpha = 50^\circ$ with $T = 1.3$ nm (denoted by the blue solid line), 5.2 nm (red), and 8.0 nm (black). The vertical dotted line indicates the excitation wavelength of Raman scattering ($\lambda = 785$ nm). (b) Raman signals from Nile blue A on the samples for p- (upper panel) and s- (lower) polarized light. The concentration of Nile blue A was 5×10^{-4} mol/l in ethanol and the samples were dried prior to the measurements. The samples were prepared at $\alpha = 50^\circ$ and $T = 1.3$ nm (blue), 5.2 nm (red), 8.0 nm (black) and 15.0 nm (orange dotted). The gray dashed curve indicates the signal from the Au thin film ($T = 50$ nm) deposited on the flat glass substrate at $\alpha = 0^\circ$. (c) Raman signals (p-polarized light) for the sample prepared at $\alpha = 50^\circ$ and $T = 8.0$ nm, with various concentrations of Nile blue A. The concentrations were 5×10^{-7} , 5×10^{-10} , and 5×10^{-12} mol/l, respectively (from top to bottom). The gray dashed curve shows the signal from Nile blue A (5×10^{-3} mol/l) on the Au thin film ($T = 50$ nm) deposited on the flat glass substrate at $\alpha = 0^\circ$. The signals in (b) and (c) are vertically shifted for the sake of clarity. (d) Signal intensity at the vibrational peak (between 577.5 and 602.5 cm^{-1}) as a function of analyte concentration. The dotted line is a guide for the eyes. The inset shows the chemical structure of Nile blue A. SERS mapping of the signal at the vibrational peak (between 577.5 and 602.5 cm^{-1}) for the sample deposited at $\alpha = 50^\circ$ with $T = 8.0$ nm for (e) p- and (f) s-polarized light. The vertical dotted lines show the intersection between the mesostructure on the MPS and that on the flat silica substrate. Note that the color scales are different in (e) and (f).

3.3 Raman scattering analysis

Figure 4 compares the optical transmission and the Raman scattering spectra of samples with different T . In the optical transmission spectra (Fig. 4(a)), the sample with $T = 1.3$ nm shows no dips for either polarization, while the sample with 5.2 (8.0) nm of Au shows a dip for p-polarized light at $\lambda = 700$ (750) nm (top panel) due to the excitation of SPPs. For s-polarized light (bottom panel), a monotonic decrease in transmission is observed for both samples toward longer wavelengths because of the increase in reflection. Figure 4(b) shows the SERS

measurement using Nile blue A (5×10^{-4} mol/l) as an analyte. The excitation wavelength of 785 nm was chosen not to overlap with the absorption band of the analyte so that the electronic transitions due to irradiation can be avoided. Notable signals, ascribable to the vibronic transitions of the molecules, are detected only for p-polarized light (top panel in Fig. 4(b)) on a broad background [40]. The signal increases with T and is largest when $T = 8.0$ nm. The number density of gaps in this sample are estimated to be $3.7/(100 \text{ nm})^2$ from the SEM image in Fig. 1(g). To attain this number density in NSL, for example, a monolayer of sphere with a radius of 27 nm is required as a mask for metal deposition. Working with such a small sphere is quite challenging in NSL, which demonstrates the advantage of the MPS-based technique. No signal appears from the flat Au surface or from the sample with $T = 15.0$ nm, neither of which possesses nanogaps. Under s-polarized light, a very small signal is observed for the samples with $T = 5.2$ and 8.0 nm (bottom panel in Fig. 4(b)) due to the presence of the nanogap in the direction orthogonal to the rods (see the SEM images in Figs. 1(e) and 1(g)).

Nile blue A with different concentrations ($5 \times 10^{-3} - 5 \times 10^{-12}$ mol/l) have been used to study the SERS dynamical range of the sample with $T = 8.0$ nm. Figure 4(c) shows the Raman spectra for the sample with the analyte concentration of 5×10^{-7} (top), 5×10^{-10} (middle), and 5×10^{-12} mol/l (bottom). The signal is observed even when the concentration is as low as 5×10^{-12} mol/l. The spectrum for the flat Au film with the analyte concentration of 5×10^{-3} mol/l shows the presence of a small peak. Taking the Au flat film as a reference, the enhancement factor of the sample is 10^9 . Figure 4(d) shows the intensity of the Raman peak (between 577.5 and 602.5 cm^{-1} , corresponds to skeletal deformations in the conjugated three-ring system [41]) versus the concentration of Nile blue A. The linear correlation from 10^{-7} to 10^{-12} mol/l suggests the large dynamical range of the present sample. Figures 4(e) and 4(f) show the spatial mappings of the SERS signal on the edge of the MPS. It is clear that the SERS signal is enhanced uniformly and selectively in the MPS region for p-polarized light, reflecting the extremely homogeneous distribution of the nanogaps.

In order to confirm the contribution of the hotspots to the SERS signal, we simulated the field distribution in the structure. The simulated optical transmission in Fig. 5(a) qualitatively reproduces the experimental data with reasonable structural parameters. Figures 5(b) and 5(c) show the field distribution in the structure irradiated with $\lambda = 785$ nm light. The field enhancement occurs between the rods for p-polarized light (Fig. 5(b)), while s-polarized light is mainly reflected at the surface of the array (Fig. 5(c)). This is in accordance with the SERS measurement where the signal enhancement occurs only for p-polarized light. Since Raman scattering is commonly performed with linearly polarized excitation sources, hot spots that are excitable at one polarization are beneficial for efficient polarization-selective sensing.

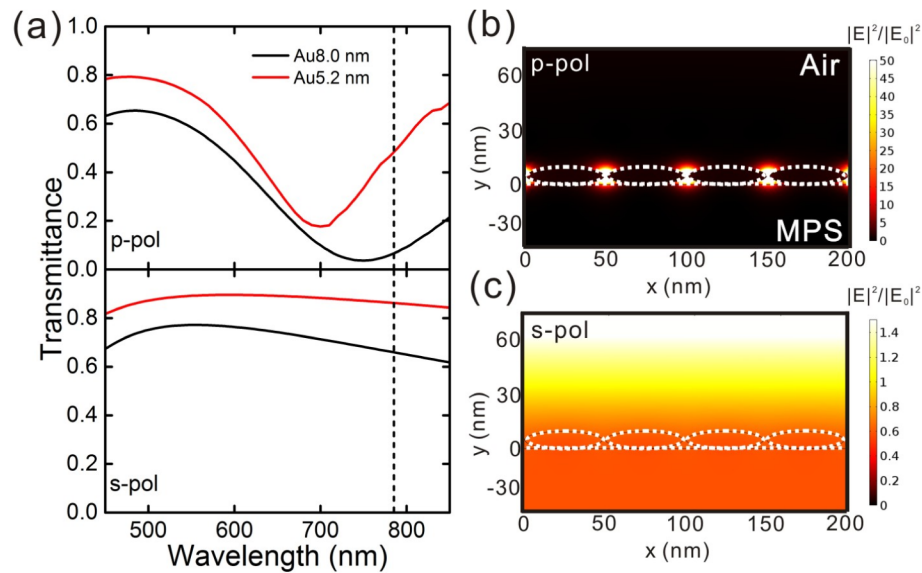


Fig. 5. (a) Simulated transmission spectra at normal incidence for p- (top panel) and s- (bottom) polarized light for the sample prepared with Au film thickness of 5.2 nm (red line) and 8.0 nm (black). The parameters of the model are: $D = 45$ nm (24 nm), $H = 10$ nm (3.5 nm), and $G = 2$ nm (4 nm) for the Au 8.0 nm (5.2 nm) sample. The vertical dotted line indicates the excitation wavelength of Raman scattering ($\lambda = 785$ nm). (b), (c) Calculated spatial distributions of the square magnitude of the electric field normalized to the incident field, $|E|^2/|E_0|^2$, in the cross section of the model simulating the Au 8.0 nm sample irradiated with light of $\lambda = 785$ nm at normal incidence for (b) p- and (c) s-polarized light. The dotted curves represent the boundaries of the materials.

4. Summary

In summary, we propose a fabrication strategy, i.e., oblique angle deposition on oriented MPS thin films with a periodic surface corrugation, for plasmonic structures one order of magnitude smaller than the light waves. The Au mesostructure is thin (< 10 nm) and the nanogap between the rods is very narrow (< 2 nm). It shows polarization selective optical transmission and SERS response due to the oriented nanogaps, where the SPPs can only be excited by p-polarized light. The polarization selectivity has practical advantages in spectroscopic applications involving linearly polarized light sources. Rubbing treatment adopted in the preparation of oriented MPS thin films is a common technique that is feasible in large-scale applications and already used in industry; thus, the present technique is a cost effective method to fabricate large-area plasmonic substrates with a high density of nanogaps uniformly distributed over a large area.

Acknowledgments

We gratefully acknowledge Dr. Hirokatsu Miyata (Canon inc.) for the supply of rubbing-treated substrates and Dr. Thang D. Dao and Dr. Satish Laxman Shinde for Raman spectroscopy. A part of this work was supported by Kyoto University Nano Technology Hub and NIMS Nanofabrication Platform in "Nanotechnology Platform Project" sponsored by the Ministry of Education, Culture, Sports, Science and Technology (MEXT), Japan. SM gratefully acknowledges a support from the construction project for the consortium of the fostering of science and technology personnel, "Nanotech Career-up Alliance (Nanotech CUPAL)".